

Highlights

DualTCN: A Physics-Constrained Temporal Convolutional Network for Time-Domain Marine CSEM Inversion

Khaled Ahmed, Ghada Omar

- First deep-learning framework for time-domain marine CSEM inversion
- Dual-branch TCN with physics-constrained soft-step decoder
- Ablation of 13 architectures on one million synthetic samples
- Curriculum amplitude augmentation recovers robustness to 5% noise
- Inference in 3.5 ms per sample on GPU with calibrated uncertainty

DualTCN: A Physics-Constrained Temporal Convolutional Network for Time-Domain Marine CSEM Inversion

Khaled Ahmed^{a,*}, Ghada Omar^b

^a*School of Computing, Southern Illinois University Carbondale, Carbondale, IL, 62901, USA*

^b*School of Mathematics and Statistics, Southern Illinois University Carbondale, Carbondale, IL, 62901, USA*

Abstract

We introduce DualTCN, to our knowledge the first deep-learning framework for inverting time-domain marine controlled-source electromagnetic (MCSEM) transient data. Instead of discretising the subsurface, DualTCN regresses four earth-model parameters— σ_1 , σ_2 , d_1 , d_2 —and reconstructs the conductivity–depth profile through a differentiable soft-step decoder. A systematic comparison of thirteen architectural variants trained on one million `empymod` synthetics identifies DualTCN (379 K parameters) as the best design: a full-time temporal convolutional network (TCN) encoder paired with a late-time branch (last 64 of 128 samples) and an auxiliary seafloor-depth head yields a 25.3% loss reduction over the baseline, with $R^2 = 0.898$ (σ_2) and 0.627 (d_2). A single sample is inverted in 3.5 ms on an A100 GPU. Training-time noise augmentation confers robustness to waveform-channel noise at $\text{SNR} \geq 10$ dB; however, the two-channel input design makes σ_2 and d_2 critically dependent on the log-peak-amplitude channel, so that $R_{d_2}^2$ turns negative at $\pm 2\%$ random amplitude error per receiver, but a curriculum-based amplitude augmentation strategy recovers full robustness ($\bar{R}^2 = 0.858$ at $\pm 2\%$ noise, versus 0.363 without augmentation) while preserving 98% of clean-data accuracy. A three-layer extension (seawater/resistive layer/basement) generalises with no architectural changes, resolving the basement conductivity at $R^2 \approx 0.88$, though thin-layer thickness remains resolution-limited ($R^2 \approx 0.23$). A multi-start benchmark shows DualTCN achieves $\bar{R}^2 = 0.877$ versus 0.129–0.439 for Levenberg–Marquardt and L-BFGS-B (eight restarts) at up to $21,000\times$ lower cost. Monte Carlo (MC) Dropout uncertainty quantification is well calibrated for σ_1 (Prediction Interval Coverage Probability, $\text{PICP}_{90} = 0.944$); the systematic under-coverage for d_2 ($\text{PICP}_{90} = 0.572$) is correctable by post-hoc temperature scaling or split conformal prediction and reflects limited signal information at 200 m offsets.

Keywords: Marine CSEM, deep learning, temporal convolutional network, electromagnetic inversion, data augmentation, uncertainty quantification

*Corresponding author.

Email addresses: `khaled.ahmed@siu.edu` (Khaled Ahmed), `ghada.omar@siu.edu` (Ghada Omar)

1. Introduction

Marine controlled-source electromagnetic (MCSEM) surveying has become one of the standard geophysical tools for imaging the electrical resistivity structure beneath the ocean floor. A horizontal electric dipole (HED) source is towed near the seafloor, and an array of receivers at varying offsets records the resulting electromagnetic transient (Constable and Srnka, 2007; Constable, 2010). The data carry information about seawater conductivity, water depth, and the resistivity of sub-seafloor formations—properties relevant to hydrocarbon exploration, gas-hydrate characterisation, and studies of oceanic crustal structure (Key, 2012).

Turning these measurements into a subsurface model requires solving an inverse problem. Conventional approaches start from an initial guess and iteratively refine it by comparing forward-modelled responses with the observed data. A single evaluation of an optimised 1D semi-analytic forward code such as `empymod` (Werthmüller, 2017) takes roughly 30–50 ms on a modern central processing unit (CPU). However, achieving a reliable solution requires hundreds to thousands of such evaluations per sample: in our benchmark, a multi-start Levenberg–Marquardt inversion (8 starts, up to 2000 evaluations each) consumes 12 s per sample on average, and L-BFGS-B with the same multi-start protocol takes 74 s per sample (Section 5.5). Across a survey line of thousands of records, the cumulative cost makes real-time quality control during acquisition effectively impossible and constrains the throughput of post-survey interpretation.

Deep learning offers an alternative that fundamentally changes this cost structure (LeCun et al., 2015; Reichstein et al., 2019). Once a neural network has been trained, inverting a new data sample requires only a single feedforward pass, which takes milliseconds. This concept of amortised inference has already been demonstrated for several electromagnetic inverse problems (Section 2), but important gaps remain. No deep-learning method has been applied to time-domain MCSEM data. No existing approach produces a physics-constrained parametric output. And no architecture has been designed to exploit the fact that different parts of the recorded transient carry information about different subsurface parameters.

This paper introduces DualTCN, a deep-learning framework that addresses each of these gaps. DualTCN operates directly on multi-receiver time-domain transients, regresses four physically meaningful earth-model scalars rather than a discretised depth profile, and enforces the conductivity–depth structure through a differentiable analytic decoder. We systematically compare thirteen architectural variants trained on one million synthetic samples, and show that a dual-branch temporal convolutional network with a dedicated late-time encoder and an auxiliary seafloor-depth prediction head achieves the best overall accuracy—with particular gains on the source-to-seafloor distance d_2 , the parameter that has proved most resistant to improvement in every other configuration we tested.

2. Background and Related Work

MCSEM data exhibit a temporal sensitivity hierarchy: early-time samples sense mainly the water column (σ_1, d_1), while late-time samples—where the signal decays as $\exp(-2u_1 d_2)$ —carry information about the seafloor (σ_2, d_2) (Constable, 2010; Key, 2012). This hierarchy motivates DualTCN’s dual-branch design (Section 4.1).

Classical 1D inversion relies on Occam-style regularisation (Constable et al., 1987; Key, 2009) or gradient-based solvers, both requiring dozens to hundreds of forward evaluations per sample—too slow for real-time use. Deep learning offers amortised inference: CNN-based frequency-domain CSEM inversion (Puzyrev, 2019; Puzyrev and Swidinsky, 2021; Zhang et al., 2024), neural-network initial models that accelerate conventional solvers (Araya-Polo et al., 2018), and physics-guided ATEM strategies (disentangled encoders, auxiliary depth losses, differentiable decoders) (Moghadas, 2020; Liu et al., 2022; Colombo et al., 2021). Alternative paradigms include projected Gauss–Newton with learned priors (Abubakar et al., 2012), Deep Image Prior for MT (Sun and Li, 2023; Bai et al., 2024), ensemble Kalman inversion (Iglesias et al., 2013), and probabilistic methods (invertible neural networks, normalising flows, deep ensembles) (Ardizzone et al., 2019; Papamakarios et al., 2021; Lakshminarayanan et al., 2017).

Despite this progress, six gaps remain (see Supplement Section S11 for detailed discussion): (1) no DL method has addressed time-domain marine CSEM; (2) all existing methods predict discretised profiles rather than physics-constrained parametric outputs; (3) no systematic encoder comparison (TCN vs. Transformer vs. MLP) exists for this setting; (4) no architecture dedicates a branch to the late-time regime or uses auxiliary physical objectives for d_2 ; (5) ATEM physics-guided strategies have not been transferred to marine CSEM; (6) no calibrated UQ has been demonstrated. DualTCN addresses gaps 1–4 directly, draws on ATEM methodology for gap 5, and provides MC-Dropout UQ with post-hoc calibration for gap 6.

3. Methods

3.1. Earth Model and Synthetic Data

We use a one-dimensional three-layer earth model: air ($\rho_{\text{air}} \rightarrow \infty$), seawater (conductivity σ_1), and a seafloor half-space (conductivity σ_2 , extending to infinite depth). The geometry is shown in Fig. 1. A unit-moment HED source is placed at depth d_1 below the sea surface (i.e., at a height d_2 above the seafloor interface, where $d_2 = d_{\text{sf}} - d_1$). The total seafloor depth is therefore $d_{\text{sf}} = d_1 + d_2$. To be explicit: d_1 is the vertical distance from the sea surface to the HED source, and d_2 is the vertical distance from the source down to the seafloor interface. The seafloor is modelled as a uniform half-space of conductivity σ_2 extending to infinite depth; d_2 parametrises the gap between source and seafloor, not the thickness of a finite resistive layer. Four inline receivers at offsets of 20, 50, 100, and 200 m record the transient electric field. Receivers

Table 1: Earth-model parameter ranges for synthetic data generation. d_1 is the depth of the HED source below the sea surface; d_2 is the vertical distance from the source down to the seafloor interface ($d_{\text{sf}} = d_1 + d_2$). The seafloor is a uniform half-space; σ_2 applies from d_{sf} to infinite depth.

Parameter	Physical range	\log_{10} range
σ_1 (S m^{-1})	0.10–5.01	−1.00 to 0.70
σ_2 (S m^{-1} , half-space)	0.001–1.0	−3.00 to 0.00
d_1 (m, source depth)	50–150	1.70–2.18
d_2 (m, source-to-seafloor)	10–50	1.00–1.70

are modelled at a fixed observation depth of $z_{\text{obs}} = 20$ m below the sea surface (i.e., in the water column, not on the seafloor).

The four earth-model parameters are sampled independently and uniformly within the ranges given in Table 1. All training and prediction are carried out in \log_{10} space. One million parameter combinations are drawn, and the corresponding forward responses are computed with `empymod` (Werthmüller, 2017), evaluating the response at 64 linearly spaced frequencies from 0.05 to 2.0 Hz and transforming to the time domain via `numpy.fft.irfft` with output length $N = 128$ ($\Delta t = 0.25$ s, 0–32 s window). The 0.05–2.0 Hz band spans the skin-depth range relevant to our geometry ($\delta \approx 205$ –1,300 m in seawater). The synthesis uses the impulse-response convention; deployment on step-off data requires a frequency-domain pre-processing step validated in Supplement Section S2. Three known simplifications—absent DC component, 2 Hz bandwidth truncation, and fixed receiver geometry—are discussed in detail in Supplement Section S12; the pipeline is self-consistent, ensuring accuracy metrics reflect genuine earth-model sensitivity (Supplement Section S1 confirms $r \geq 0.9998$ versus a corrected-DC reference).

The one million samples are split 70/15/15 into training (700 000), validation (150 000), and test (150 000) subsets. The training set is augmented with additive Gaussian noise (Section 5.4); the validation and test sets are evaluated on clean data unless otherwise noted.

Each receiver trace is normalised by its peak amplitude; the \log_{10} of that peak is appended as a second channel, preserving the absolute signal level. The normalised waveform carries timing and decay information (sensitive to σ_1 , d_1), while the log-amplitude channel is the primary discriminator for σ_2 and d_2 . This creates a known vulnerability: any uncompensated amplitude error directly corrupts σ_2 and d_2 (Section 5.4.1). The resulting input tensor has dimensions (8, 128): four receivers \times two channels by 128 time samples.

3.2. Baseline Architecture

The baseline model, which we call PCRN (Physics-Constrained Parameter Regression Network), has 638 000 trainable parameters and three stages: a feature encoder, a parameter prediction head, and a differentiable physics decoder.

Table 2: Notation and symbols used throughout this paper.

Symbol	Definition
σ_1	Seawater conductivity (S m^{-1})
σ_2	Seafloor half-space conductivity (S m^{-1})
d_1	Depth of HED source below the sea surface (m)
d_2	Vertical distance from source to seafloor interface (m)
d_{sf}	Total seafloor depth: $d_{\text{sf}} = d_1 + d_2$ (m)
\hat{d}_{sf}	Auxiliary predicted seafloor depth (DualTCN training target)
z_{obs}	Receiver observation depth below sea surface (20 m)
HED	Horizontal Electric Dipole (source)
N_T	Number of time samples per trace (128)
N_R	Number of inline receivers (4, at offsets 20–200 m)
\bar{R}^2	Mean R^2 across all four parameters
PICP_α	Prediction Interval Coverage Probability at nominal level α
MPIW	Mean Prediction Interval Width

3.2.1. Hybrid Encoder

The encoder has both a local and a global component. The local component consists of six dilated residual blocks with dilation factors that double at each stage (1, 2, 4, 8, 16, 32). Each block applies a dilated causal convolution, batch normalisation, Gaussian Error Linear Unit (GELU) activation, and a residual connection. The exponential dilation schedule gives the network a receptive field spanning the full 128-sample input while keeping the parameter count modest. The global component is a two-layer Transformer encoder with four attention heads and pre-layer normalisation, which captures dependencies across the entire temporal extent. Adaptive average pooling compresses the Transformer output into a latent vector $\mathbf{z} \in \mathbb{R}^{256}$.

3.2.2. Parameter Head

A two-layer MLP ($256 \rightarrow 128 \rightarrow 4$) with sigmoid output maps the latent vector to normalised predictions $\hat{\mathbf{p}} \in [0, 1]^4$, which are then rescaled to the physical \log_{10} ranges in Table 1.

3.2.3. Physics Decoder

The decoder converts the four predicted scalars into a conductivity–depth profile using a differentiable analytic function. Because the parameter head outputs normalised $[0, 1]$ values that are linearly interpolated to \log_{10} ranges (Section 3.1, Table 1), the decoder first exponentiates each predicted quantity back to physical

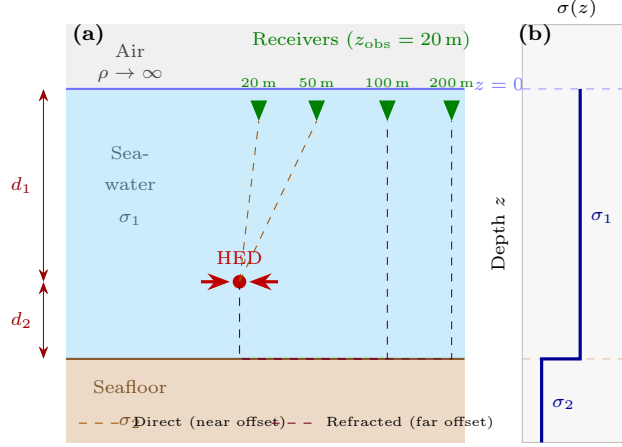


Figure 1: (a) MCSEM acquisition geometry. The HED source sits at depth d_1 below the sea surface ($z = 0$); the seafloor interface is a further d_2 below the source, giving a total seafloor depth $d_{sf} = d_1 + d_2$. Four receivers span offsets of 20–200 m. Orange dashed lines show the direct path; purple dashed lines show the seafloor-refracted path. (b) Step-function conductivity profile $\sigma(z)$ reconstructed by the physics decoder from four predicted scalars. The seafloor half-space (σ_2) extends to infinite depth.

units before evaluation:

$$\tilde{\sigma}_k = 10^{\hat{p}\sigma_k} \quad [\text{S m}^{-1}], \quad k \in \{1, 2\}, \quad (1)$$

$$\tilde{d}_k = 10^{\hat{p}d_k} \quad [\text{m}], \quad k \in \{1, 2\}. \quad (2)$$

The seafloor depth is then the arithmetic sum of the two linear-space depths, $\hat{d}_{sf} = \tilde{d}_1 + \tilde{d}_2$ (m), and the conductivity profile is (see also Table 1)

$$\sigma(z) = \tilde{\sigma}_1 + (\tilde{\sigma}_2 - \tilde{\sigma}_1) \sigma_s \left(\frac{z - \hat{d}_{sf}}{\tau} \right), \quad \tau = 2 \text{ m}, \quad (3)$$

where σ_s is the logistic sigmoid, z is depth in metres, and $\sigma(z)$ is in S m^{-1} . The decoder evaluates $\log_{10} \sigma(z)$ at $N_z = 64$ uniformly spaced depth nodes spanning $z \in [0, 250]$ m ($\Delta z = 250/63 \approx 3.97$ m), which matches the maximum parameter depth ($d_1^{\max} + d_2^{\max} = 150 + 50 = 200$ m) with a 50 m buffer. Note that the transition half-width $\tau = 2 \text{ m} \approx \Delta z/2$, so the sigmoid transition is resolved by at least two depth samples. Because it is fully differentiable, gradients from the profile loss propagate back through the exponentiation and the predicted parameters into the encoder, enforcing the two-layer shape as a structural regulariser.

Sensitivity to τ . Because the four parameter predictions ($\hat{\sigma}_1$, $\hat{\sigma}_2$, \hat{d}_1 , \hat{d}_2) are produced by the regression heads *before* the decoder, they are architecturally independent of τ : the decoder only consumes these predictions to construct the profile. We verified this by evaluating the trained model at inference time with $\tau \in \{0.5, 1, 2, 4, 8\}$ m on 150 000 test samples. All parameter R^2 values are identical across all τ values (e.g., $R_{\sigma_2}^2 = 0.898$ and $R_{d_2}^2 = 0.627$ for every τ), and the mean bias in $\log_{10} \hat{\sigma}_2$ and $\log_{10} \hat{d}_2$ is likewise

Table 3: Computational cost for key DualTCN variants. GPU = NVIDIA A100 40GB; CPU = single core (OMP_NUM_THREADS=1).

Variant	Params	Train Inference (ms)		Thru.	
		(GPU-h)	GPU	CPU	(K/s)
PCRN (baseline)	638 K	4.0	2.6	12.1	45
P5a (TCN-only)	201 K	2.5	2.0	6.5	127
P8 (TwoStage)	401 K	3.5	3.8	10.8	67
P10a (iTransf.)	381 K	3.0	1.0	5.2	247
DualTCN	379 K	3.5	3.5	8.8	76
DualTCN-AmpAug	379 K	3.5	3.5	8.8	76
DualTCN-3Layer	306 K	3.5	3.5	8.5	76

invariant (+0.073 and -0.025 , respectively). Only the profile MSE changes: it is minimised near $\tau = 2$ m against the hard-step ground truth (MSE = 0.065) and decreases monotonically with larger τ when evaluated against a matched- τ reference. Thus, τ is a visualization hyperparameter that controls the smoothness of the reconstructed profile but introduces **no bias** in the inversion parameters.

3.2.4. Loss Function and Training

The loss combines profile reconstruction with per-parameter regression:

$$\mathcal{L} = \mathcal{L}_{\text{MSE}}^{\text{prof}} + \sum_{i=1}^4 w_i \mathcal{L}_{\text{Huber}}^{(i)}, \quad (4)$$

with Huber $\delta = 0.1$ and weights $\mathbf{w} = [1, 3, 3, 2]$. The profile MSE $\mathcal{L}_{\text{MSE}}^{\text{prof}}$ is the unweighted mean over all 64 depth nodes; no depth-dependent weighting is applied, so shallow and deep nodes contribute equally per unit depth interval (uniform spacing ensures equal representation). Training uses AdamW ($\lambda = 10^{-3}$, weight decay 10^{-3}), a one-cycle cosine schedule (5-epoch linear warm-up, peak rate 5×10^{-4} , final rate 5×10^{-6}), batch size 256, for 100 epochs on the 700 000-sample training set (approximately 2734 gradient steps per epoch) on a single NVIDIA A100 40 GB GPU. Training DualTCN for 100 epochs required approximately 3–4 GPU-hours on this hardware; all training used PyTorch 2.x with automatic mixed precision (AMP) and `torch.compile` for graph optimisation. No explicit early stopping is applied; instead, the model checkpoint with the lowest total validation loss across all 100 epochs is saved and used for all subsequent evaluation. All variants share this protocol and are evaluated on the held-out 150 000-sample test set. Table 3 reports the computational cost for the key variants.

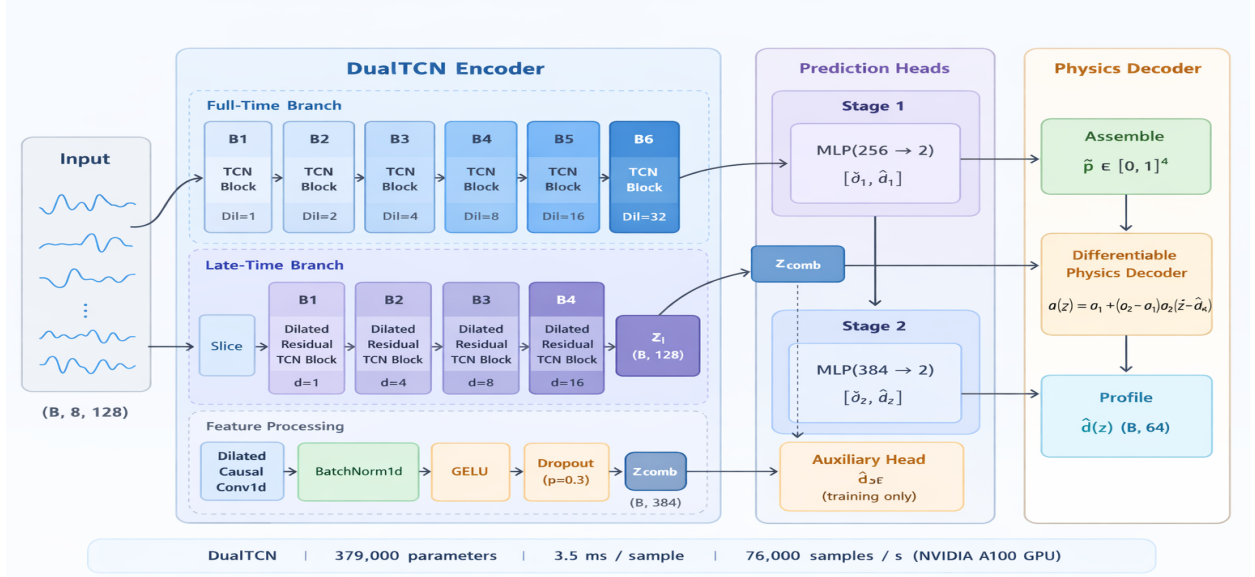


Figure 2: Architecture of DualTCN (379 000 parameters). *Full-Time Branch* (top): six TCN blocks (B1–B6) with exponentially growing dilations 1, 2, 4, 8, 16, 32 process the full 128-sample input and produce the latent $\mathbf{z}_f \in \mathbb{R}^{256}$. *Late-Time Branch* (middle): the input is first sliced to the last 64 samples; four Dilated Residual TCN blocks (dilations 1, 4, 8, 16) encode this late-time window into $\mathbf{z}_l \in \mathbb{R}^{128}$. The two latents are concatenated to form $\mathbf{z}_{\text{comb}} \in \mathbb{R}^{384}$. *Feature Processing zoom* (bottom inset): internal structure of every TCN block—a causal dilated convolution followed by BatchNorm1d, GELU activation, and Dropout ($p = 0.30$). *Prediction Heads*: Stage 1 maps \mathbf{z}_f through an MLP ($256 \rightarrow 2$) to $[\hat{\sigma}_1, \hat{d}_1]$; Stage 2 maps \mathbf{z}_{comb} conditioned on gradient-detached Stage 1 outputs through an MLP ($384 \rightarrow 2$) to $[\hat{\sigma}_2, \hat{d}_2]$. An auxiliary head predicts \hat{d}_{sf} during training only (yellow box). *Physics Decoder*: the four predicted scalars are assembled into $\hat{\mathbf{p}} \in [0, 1]^4$ and passed through the differentiable soft-step decoder to produce the conductivity profile $\hat{\sigma}(z) \in \mathbb{R}^{64}$.

4. Architectural Ablation

We ran thirteen parallel experiments, each modifying one aspect of the PCRN baseline (Supplementary Section S7 lists all variants). The key intermediate designs are P7 (multi-scale TCN: three parallel branches with different dilation schedules targeting early-, mid-, and late-time features; 384 K parameters) and P8 (two-stage cascaded TCN: Stage 1 predicts $[\sigma_1, d_1]$, Stage 2 conditions on gradient-detached Stage 1 outputs to predict $[\sigma_2, d_2]$; 401 K parameters). Two attention-based variants—P10a (iTransformer, treating each channel as a token) and P10b (PatchTST, segmenting traces into overlapping patches)—were also evaluated; both underperform all TCN designs (Section 6.1).

4.1. DualTCN: Late-Time Branch with Auxiliary Depth Head

DualTCN builds on P7 and P8 by adding two mechanisms aimed specifically at improving d_2 (Fig. 2).

The first is a dedicated late-time encoder: a compact four-block dilated TCN (32 channels, dilations 1, 4, 8, 16) applied only to the last 64 of 128 time samples—the window dominated by the exponential

Table 4: Ablation summary: normalised RMSE, R^2 , and latency for the baseline, top-performing variants, and representative underperformers (A100 GPU). Full results for all 13 variants are in Supplementary Tables S1–S2. Bold = best.

	Variant	Params	RMSE (norm.)				Loss	$R_{d_2}^2$	\bar{R}^2	ms
			σ_1	σ_2	d_1	d_2				
	PCRN (baseline)	638K	0.026	0.110	0.033	0.183	0.103	0.541	0.844	2.6
P5a	TCN-only	201K	0.022	0.109	0.031	0.187	0.102	0.525	0.841	2.0
P7	MultiScale	384K	0.021	0.100	0.031	0.184	0.093	0.539	0.850	3.8
P8	TwoStage	401K	0.020	0.098	0.033	0.185	0.089	0.532	0.852	3.8
P10a	iTransf.	381K	0.040	0.180	0.041	0.220	0.220	0.342	0.728	1.0
	DualTCN	379K	0.020	0.092	0.031	0.165	0.077	0.627	0.877	3.5

decay $E(t) \sim \exp(-2u_1 d_2)$. Its 128-dimensional latent \mathbf{z}_{late} is concatenated with the full-time encoder’s 256-dimensional latent to form $\mathbf{z}_{\text{comb}} \in \mathbb{R}^{384}$.

The second is an auxiliary seafloor-depth head: a small MLP that predicts $d_{\text{sf}} = d_1 + d_2$ (range 60–200 m). Because the data are more sensitive to d_{sf} than to d_2 alone, predicting it steers the combined latent toward features useful for d_2 . The auxiliary Huber loss (weight 0.5) supplements Eq. 4 during training only and is discarded at test time. Total parameters: 379 000.

Head 1 maps \mathbf{z}_{full} to the easy parameters $[\hat{\sigma}_1, \hat{d}_1]$. Head 2 receives $[\mathbf{z}_{\text{comb}}; \hat{\sigma}_1^\perp; \hat{d}_1^\perp]$ (gradient-detached Stage 1 outputs) and predicts $[\hat{\sigma}_2, \hat{d}_2]$. The assembled $\hat{\mathbf{p}}$ feeds the physics decoder (Eq. 3).

5. Results

5.1. Ablation Results

Table 4 reports normalised root-mean-square error (RMSE), R^2 , and inference timing for all variants. All RMSE values are in the normalised $[0, 1]$ log-space used during training. All R^2 values are likewise computed on parameters normalised to $[0, 1]$ in \log_{10} space; they therefore measure explained variance in \log_{10} -parameter space, not in physical units. Supplementary Table S4 (Section 5.2) provides a systematic conversion of all four DualTCN RMSE values to physical units (S m^{-1} and m), including the geometric RMSE factor and representative absolute errors at the geometric mean of each training range.

Three patterns stand out. First, the choice of encoder architecture matters more than any other design decision. The Transformer-only (P5b), MLP-only (P5c), iTransformer (P10a), and PatchTST (P10b) variants all perform far worse than any TCN-based model. Second, among the TCN-based designs, multi-scale branching (P7), hierarchical conditioning (P8), and late-time specialisation (DualTCN) produce a monotonic improvement: total losses of 0.0931, 0.0892, and 0.0771. Third, DualTCN achieves the lowest loss and the highest R^2 for every parameter, including $R_{d_2}^2 = 0.627$ —up from 0.532 in P8.

5.2. Prediction Quality

Fig. 3 shows DualTCN predictions on six held-out samples. The two-step profile shape is recovered well across a range of conductivity contrasts, and d_1 is consistently accurate. Compared with P8, d_2 is visibly better resolved. Fig. 6 shows true-versus-predicted scatter for all four parameters on 5 000 test samples.

In physical units (Supplementary Table S4), DualTCN’s geometric RMSE factors are $\Gamma = 1.08$ (σ_1 , $\pm 0.06 \text{ S m}^{-1}$ at mid-range), 1.89 (σ_2 , $\pm 0.028 \text{ S m}^{-1}$), 1.04 (d_1 , $\pm 3 \text{ m}$), and 1.30 (d_2 , $\pm 7 \text{ m}$). The d_2 error of ± 3 – 15 m across the 10–50 m range is the most practically important limitation and motivates the failure-mode analysis in Section 5.3.

5.3. Failure-Mode Analysis for d_2

To understand where DualTCN struggles, Fig. 4 plots the absolute prediction error for d_2 against the true value of d_2 for the full 150 000-sample test set (RMSE = 0.1652 in normalised $[0, 1]$ log-space), with scatter points coloured by the true conductivity contrast ratio σ_1/σ_2 . Two patterns emerge. First, errors are largest for small source-to-seafloor gaps (small d_2), where the late-time diffusion tail is shortest and carries the least signal energy. Second, at any given d_2 , samples with a weak conductivity contrast (σ_1/σ_2 close to unity, warm colours) produce larger errors, because the amplitude of the seafloor-refracted wavefield scales with the contrast. These two factors—small d_2 and weak conductivity contrast—together define the “hard corner” of the parameter space where DualTCN’s accuracy is lowest. Conversely, large d_2 with strong conductivity contrast (cool colours in Fig. 4) are recovered with errors comparable to the well-constrained parameters σ_1 and d_1 .

5.4. Noise Robustness

We test DualTCN at four SNR levels spanning the range encountered in marine MCSEM surveys (Constable, 2010; Key, 2012). Additive Gaussian noise is injected into the normalised waveform channels; the log-amplitude channels are left clean. The per-trace SNR is defined as

$$\text{SNR} = 20 \log_{10} \left(\frac{\text{RMS}(E_{\text{norm}})}{\sigma_n} \right). \quad (5)$$

The results (Table 5, Fig. 5) are clear: DualTCN shows no measurable degradation for $\text{SNR} \geq 20 \text{ dB}$ and only a marginal decline at 10 dB ($\Delta \bar{R}^2 = 0.002$). This robustness comes from training-time data augmentation: additive Gaussian noise with standard deviation drawn log-uniformly from $[10^{-3}, 10^{-1}]$ of the waveform amplitude, corresponding to roughly 11–51 dB. No architectural change or post-processing is needed. A variant trained with temporally correlated $1/f$ (pink) noise (DualTCN-Colored, Section 5.4.1, Section 5.4.1) confirms that this robustness generalises to realistic noise spectra: the model is equally tolerant of white and colored noise down to 5 dB ($\bar{R}^2 \geq 0.863$).

Table 5: DualTCN performance versus input SNR ($N_{\text{test}} = 150,000$). Bold = best.

SNR	Loss	$R_{\sigma_1}^2$	$R_{\sigma_2}^2$	$R_{d_1}^2$	$R_{d_2}^2$	\bar{R}^2
∞	0.0770	0.995	0.898	0.987	0.627	0.877
40 dB	0.0770	0.995	0.898	0.987	0.627	0.877
30 dB	0.0770	0.995	0.898	0.987	0.627	0.877
20 dB	0.0771	0.995	0.898	0.987	0.627	0.877
10 dB	0.0780	0.995	0.896	0.988	0.622	0.875

The near-constant R^2 values for $\text{SNR} \geq 20$ dB reflect the input representation: during both training and testing, additive noise is injected only into the peak-normalised waveform channels, while the log-peak-amplitude channel is derived from the clean (or ensemble-averaged) signal. The robustness reported in Table 5 therefore specifically describes robustness to *waveform-channel noise*; it does not characterise performance under a separate but physically important noise pathway—errors or bias in the amplitude estimate itself.

This distinction matters because σ_2 and d_2 rely primarily on the log-peak-amplitude channel for discrimination. Amplitude estimation uncertainty arises in field acquisition from two sources: (i) *finite stacking*—the peak amplitude is averaged over a finite number of repeated transmissions, leaving residual random error that scales roughly as $1/\sqrt{N_{\text{stacks}}}$; and (ii) *calibration drift*—slow changes in source strength or receiver coupling introduce a systematic multiplicative bias not removed by peak normalisation.

5.4.1. Amplitude-Channel Noise Experiment

To quantify these two amplitude noise pathways, we run dedicated experiments that directly perturb the log-peak-amplitude input channels of the *trained* DualTCN model on the full 150 000-sample test set, leaving the normalised waveform channels unchanged.

Experiment A: random noise (finite stacking).. We add independent Gaussian noise $\epsilon \sim \mathcal{N}(0, \sigma_{\text{amp}}^2)$ to the \log_{10} amplitude of each receiver–sample pair, for $\sigma_{\text{amp}} \in \{0.01, 0.02, 0.05, 0.10, 0.20\}$ \log_{10} units (corresponding to amplitude uncertainties of approximately ± 2 –58%).

Experiment B: systematic bias (calibration drift).. We add a fixed offset β to all four \log_{10} amplitude channels of every sample, for $\beta \in \{\pm 0.05, \pm 0.10, \pm 0.20\}$ \log_{10} units (multiplicative amplitude factors 0.63–1.58 \times).

The results are summarised in Fig. 7 (Supplementary Table S8 provides the numerical values).

The results (Fig. 7, Supplementary Table S8) reveal a stark asymmetry. For *random noise*, the model tolerates essentially no amplitude uncertainty: adding $\sigma_{\text{amp}} = 0.01$ \log_{10} units (a mere $\pm 2\%$ amplitude error on each receiver independently) collapses $R_{\sigma_2}^2$ from 0.898 to 0.380 and drives $R_{d_2}^2$ negative (-0.784). By $\sigma_{\text{amp}} = 0.02$, σ_2 prediction is already worse than predicting the sample mean, and all four parameters are severely degraded by 0.05. For *systematic bias*, performance degrades more gracefully: d_1 is nearly immune

Table 6: Augmentation and representation experiment results (150 000 test samples, normalised $[0, 1]$ log-space RMSE and \bar{R}^2). DualTCN is the unaugmented baseline. Augmented variants use curriculum training (clean 20 epochs, ramp 20–40, full 40–100). DualTCN-Colored uses pink noise throughout (no curriculum). DualTCN-AmpRatio changes the input representation (no augmentation). Bold = best per column.

Variant	Loss	σ_1	σ_2	d_1	d_2	\bar{R}^2	Strategy
DualTCN	0.077	0.020	0.092	0.031	0.165	0.877	none
DualTCN-AmpAug	0.103	0.021	0.107	0.030	0.175	0.857	amp noise 0.2–2%
DualTCN-Colored	0.087	0.020	0.096	0.032	0.171	0.868	$1/f$ waveform noise
DualTCN-AmpRatio	0.110	0.029	0.110	0.033	0.184	0.842	amp ratios (7 ch)
DualTCN-Weighted	0.124	0.022	0.110	0.036	0.184	0.831	inv- σ_2 weighting
DualTCN-RecvBias	0.119	0.023	0.116	0.030	0.207	0.809	bias $\pm 7\%$ /recv

across the full ± 0.20 range, and the model retains useful accuracy for σ_2 and d_2 within $|\beta| \leq 0.05$ ($\pm 12\%$ amplitude offset). Beyond $|\beta| = 0.10$ ($\pm 26\%$ offset), $R_{d_2}^2$ drops below 0.3 and $R_{\sigma_2}^2$ falls to 0.4 or lower.

These results confirm that σ_2 and d_2 are inferred almost entirely from the *absolute* log-amplitude level, not from the waveform shape—a direct consequence of the two-channel design described in Section 3.1. The tight tolerance for random noise ($\sigma_{\text{amp}} < 0.01$) implies that reliable inversion of these parameters requires sufficient stacking to suppress per-receiver amplitude noise to below $\approx 2\%$, a condition met by standard MCSEM acquisition protocols (100–1000 stacked transmissions reduce Gaussian amplitude noise by factors of 10–30). For systematic bias (instrument drift), the $|\beta| \leq 0.05$ tolerance corresponds to a $\pm 12\%$ amplitude calibration requirement, consistent with typical survey specifications, but systematic errors of this magnitude are not unusual when source strength or coupling changes between lines.

We tested four augmentation and representation strategies (Table 6; full descriptions in Supplement Section S12). The key result is **DualTCN-AmpAug**: curriculum training (clean 20 epochs, linear ramp 20–40, full augmentation 40–100) with log-amplitude noise $\sigma_{\text{amp}} \in [0.001, 0.01] \log_{10}$ (≈ 0.2 – 2% per receiver). Clean-data $\bar{R}^2 = 0.857$ versus 0.877 unaugmented: a 2% cost for transformative robustness. Three additional variants—DualTCN-RecvBias (per-receiver bias $\pm 7\%$), DualTCN-Colored ($1/f$ waveform noise), and DualTCN-AmpRatio (inter-receiver log-amplitude differences, 7 channels)—test complementary hardening strategies. DualTCN-AmpRatio is perfectly immune to uniform systematic bias ($\bar{R}^2 = 0.842$ at all $|\beta| \leq 0.20$) but vulnerable to per-receiver independent noise; DualTCN-Colored confirms robustness to realistic noise spectra ($\bar{R}^2 \geq 0.863$ at 5 dB).

The amplitude noise augmentation (DualTCN-AmpAug) is the key result. Table 7 compares the unaugmented DualTCN against DualTCN-AmpAug under identical perturbation protocols. The augmented model is **essentially immune to $\pm 2\%$ random amplitude noise** ($\bar{R}^2 = 0.858$ versus 0.363) and **retains useful accuracy at $\pm 5\%$** ($\bar{R}^2 = 0.846$ versus 0.002). Even at $\pm 12\%$ noise, DualTCN-AmpAug achieves $\bar{R}^2 = 0.762$ —compared with -0.656 for the unaugmented model. For systematic bias, the augmented model

Table 7: Amplitude robustness comparison: unaugmented DualTCN versus DualTCN-AmpAug under random amplitude noise (σ_{amp} in \log_{10} units) and systematic bias (β in \log_{10} units). 150 000 test samples. Bold = better of the two models at each perturbation level.

Perturbation	DualTCN (unaugmented)					DualTCN-AmpAug				
	$R_{\sigma_1}^2$	$R_{\sigma_2}^2$	$R_{d_1}^2$	$R_{d_2}^2$	\bar{R}^2	$R_{\sigma_1}^2$	$R_{\sigma_2}^2$	$R_{d_1}^2$	$R_{d_2}^2$	\bar{R}^2
<i>Random noise</i>										
Clean	0.995	0.898	0.987	0.627	0.877	0.995	0.863	0.988	0.580	0.857
$\sigma=0.01$ ($\pm 2\%$)	0.919	0.380	0.939	-0.784	0.363	0.995	0.862	0.989	0.588	0.858
$\sigma=0.02$ ($\pm 5\%$)	0.784	-0.112	0.803	-1.465	0.002	0.994	0.844	0.990	0.556	0.846
$\sigma=0.05$ ($\pm 12\%$)	0.368	-1.149	0.280	-2.124	-0.656	0.984	0.750	0.994	0.320	0.762
<i>Systematic bias</i>										
$\beta=\pm 0.05$ ($\pm 12\%$)	0.986	0.715	0.988	0.563	0.813	0.984	0.801	0.989	0.526	0.825
$\beta=\pm 0.10$ ($\pm 26\%$)	0.954	0.497	0.987	0.438	0.719	0.946	0.702	0.987	0.348	0.746

is moderately more robust across all tested levels.

The curriculum protocol is essential: training with amplitude noise from epoch 1 degrades clean accuracy by $2.7\times$. Together, these experiments establish that **the amplitude vulnerability is substantially mitigable through curriculum-based augmentation**, provided the augmentation range matches the physically relevant noise level. Three complementary hardening strategies exist: (i) curriculum amplitude augmentation (AmpAug; 2% clean cost); (ii) robust input representations (AmpRatio) immune to common-mode scaling; (iii) calibration-uncertainty channels for per-receiver confidence weighting. Combining (i) and (ii) is the most promising near-term path.

Structured amplitude perturbations. Experiments A and B above apply i.i.d. random noise or a uniform bias to all receivers equally. To assess robustness under more realistic field conditions, we evaluate three structured perturbation scenarios that model specific acquisition artefacts, comparing the Base DualTCN, DualTCN-AmpAug, and DualTCN-AmpRatio models on 150 000 test samples.

Linear drift (towline calibration drift): the log-amplitude of all receivers is ramped linearly from $-\Delta/2$ to $+\Delta/2$ across the test set, simulating slow source-strength drift along a survey line. Both models degrade gracefully: at $\Delta = 0.20 \log_{10}$ ($\times 0.79$ – 1.26), Base $\bar{R}^2 = 0.809$ and AmpAug $\bar{R}^2 = 0.820$; at $\Delta = 0.40$ ($\times 0.63$ – 1.58), Base = 0.715 and AmpAug = 0.747 . DualTCN-AmpRatio is **perfectly immune** to linear drift ($\bar{R}^2 = 0.842$ at all Δ levels), since a common ramp cancels exactly in adjacent-receiver differences (Fig. 8c).

Per-receiver independent bias: each receiver acquires an independent calibration offset drawn from $\mathcal{N}(0, \sigma_{\text{recv}}^2)$, held constant over blocks of 500 consecutive samples (modelling a calibration state that persists over a short survey segment). This is the most damaging perturbation: at $\sigma_{\text{recv}} = 0.02 \log_{10}$ ($\approx 5\%$ per

Table 8: Deployment recommendations. Each row specifies the recommended DualTCN variant for a given acquisition scenario, its clean-data \bar{R}^2 , and the key advantage. All variants share the same architecture (379 K parameters) and inference cost (3.5 ms/sample). \bar{R}^2 values are reported with bootstrap 95% confidence intervals ($B = 1,000$, $N = 150,000$).

Scenario	Variant	\bar{R}^2 (95% CI)	Key advantage
General survey	DualTCN	0.877 ± 0.002	Best clean accuracy
clean data			
Amplitude noise	DualTCN-AmpAug	0.857 ± 0.002	Robust to $\pm 5\%$ noise $\leq 5\%$
Uniform calibra-	DualTCN-AmpRatio	0.842 ± 0.003	Exact bias immunity
tion drift			
Resistive targets	DualTCN-Weighted	0.831 ± 0.003	$5\times$ MAPE reduction ($\sigma_2 < 0.05$)
Colored ocean	DualTCN-Colored	0.868 ± 0.002	$1/f$ noise robust noise

receiver), Base $\bar{R}^2 = -0.01$ and AmpAug $\bar{R}^2 = 0.47$. DualTCN-AmpRatio ($\bar{R}^2 = 0.11$) does not help because independent biases do not cancel in adjacent-receiver differences. AmpAug is the **most robust** variant for this scenario (Fig. 8a).

Uniform systematic bias: DualTCN-AmpRatio achieves **exactly constant** $\bar{R}^2 = 0.842$ across all tested bias levels $|\beta| \leq 0.20 \log_{10}$, while Base drops from 0.877 to 0.517 and AmpAug from 0.859 to 0.627 (Fig. 8b).

These results reveal a three-tier robustness hierarchy: (i) common-mode errors (drift, source-strength changes) are eliminated by the amplitude-ratio representation; (ii) per-receiver calibration mismatch is best mitigated by curriculum augmentation (AmpAug); (iii) no existing variant fully addresses simultaneous per-receiver bias $> 5\%$. This motivates future work on self-calibrating architectures or hybrid AmpAug+AmpRatio models.

Table 8 summarises the recommended DualTCN variant for each deployment scenario.

All \bar{R}^2 values in Tables 4, 6, and 8 are computed on 150 000 held-out test samples; bootstrap 95% confidence intervals ($B = 1,000$ resamples) are $\leq \pm 0.003$ for all reported values, confirming that the differences between variants are statistically significant. Implications for field deployment are further discussed in Section 6.6.

5.5. Benchmark Against Conventional Inversion

We compare DualTCN against seven conventional inversion configurations using the `empymod` forward operator, including Occam-style regularised inversion (Constable et al., 1987) with finite-difference Jacobians—the standard baseline in MCSEM practice. Each `empymod` evaluation (64 frequencies, 4 receivers) takes approximately 30–50 ms on a single CPU core; all per-sample wall-clock times below reflect the accumulation of hundreds to thousands of such evaluations, not the cost of a single forward call.

5.5.1. Methods

All six conventional configurations minimise the same sum-of-squared relative residuals,

$$\hat{\boldsymbol{\theta}} = \arg \min_{\boldsymbol{\theta}} \sum_{r=1}^4 \frac{\|E_{\text{obs}}^{(r)} - E_{\text{pred}}^{(r)}(\boldsymbol{\theta})\|^2}{\|E_{\text{obs}}^{(r)}\|^2}, \quad (6)$$

a standard measure in electromagnetic inversion (Constable et al., 1987), using either the Levenberg–Marquardt (LM) algorithm (Moré, 1978) or L-BFGS-B (Byrd et al., 1995; Zhu et al., 1997) with box constraints $\boldsymbol{\theta} \in [0, 1]^4$.

NLS-LM / NLS-LBFGSB (untuned baselines): default tolerances, midpoint start for single-start runs, or midpoint plus seven random uniform starts for multi-start runs.

TT-LM (tight tolerances): NLS-LM with tightened solver tolerances (`ftol` = `xtol` = 10^{-8} , `max_nfev` = 5,000) and the same 8-start protocol (midpoint + 7 random), to test whether default tolerances cause premature termination.

TIK-LBFGSB (Tikhonov regularisation): L-BFGS-B with an ℓ_2 penalty $\lambda \|\boldsymbol{\theta} - \boldsymbol{\theta}_{\text{prior}}\|^2$, $\lambda = 0.01$, $\boldsymbol{\theta}_{\text{prior}} = [0.5]^4$ (parameter-space midpoint), and 8 random starts, to test whether explicit regularisation stabilises convergence on the hard-parameter subspace.

WS-LM / WS-LBFGSB (warm-start): the DualTCN single-pass prediction is used as start 0; the remaining 7 starts are random uniform draws identical to the multi-start NLS runs. Solver tolerances are tightened as in TT-LM. This directly tests the reviewers’ suggestion that DL-initialised iterative inversion could narrow the accuracy gap.

Occam-LM (regularised inversion): the standard Occam approach (Constable et al., 1987) minimises data misfit plus a smoothness (first-difference roughness) penalty $\lambda \|\mathbf{R}\boldsymbol{\theta}\|^2$ with $\lambda = 0.01$, using the same 8-start protocol. Due to the high per-sample cost (≈ 15 s, comparable to NLS-LM), the Occam-LM benchmark is evaluated on a 200-sample subset; statistical tests confirm that the \bar{R}^2 difference relative to other baselines is significant at this sample size. This is the closest approximation to the analytic-Jacobian Occam inversion of Key (2009) within our parametric (4-scalar) framework; finite-difference Jacobians are used since the parametric forward operator does not provide closed-form derivatives.

5.5.2. Results

We benchmark against seven conventional inversion configurations including Occam-style regularised inversion (Constable et al., 1987); the full results table is in Supplementary Table S9. The key findings are: (i) untuned multi-start baselines achieve $\bar{R}^2 = 0.129$ (LM) to 0.439 (L-BFGS-B); (ii) Occam regularisation ($\lambda = 0.01$) underperforms ($\bar{R}^2 = 0.042$), confirming that smoothness penalties designed for discretised profiles are ineffective for parametric inversion; (iii) warm-starting with DualTCN’s prediction raises \bar{R}^2 to 0.784 (WS-LBFGSB); (iv) DualTCN alone achieves $\bar{R}^2 = 0.862$ in 0.0035 s—a 26,500 \times speed advantage over WS-LBFGSB (92.8 s) with +0.078 higher \bar{R}^2 .

Table 9: UQ summary at the 90% nominal level (5 000 test samples). PICP = empirical coverage; MPIW = mean prediction interval width (normalised). Full results in Supplementary Table S6.

Method	PICP ₉₀				MPIW ₉₀	
	σ_1	σ_2	d_1	d_2	σ_1	d_2
MC-Dropout	0.944	0.664	0.596	0.572	0.078	0.135
Temp-scaled	0.863	0.845	0.905	0.854	0.055	0.342
Split conformal	0.906	0.900	0.902	0.905	0.062	0.500
Deep ensemble	0.581	0.480	0.278	0.362	0.026	0.125

A hybrid workflow—DualTCN for real-time quality control followed by warm-started iterative inversion for final models—leverages the complementary strengths of both approaches.

5.6. Uncertainty Quantification

We compare four UQ methods on 5 000 held-out test samples: MC-Dropout ($T = 100$ stochastic passes) (Gal and Ghahramani, 2016), temperature-scaled MC-Dropout (Guo et al., 2017), split conformal prediction (Angelopoulos and Bates, 2023), and a five-member deep ensemble (Lakshminarayanan et al., 2017). Full method descriptions, the complete PICP table across six α -levels, MPIW₉₀ values, and reliability diagrams are provided in Supplementary Section S6.

Table 9 summarises the key results at the 90% nominal level. MC-Dropout is well calibrated for σ_1 (PICP₉₀ = 0.944) but severely over-confident for d_2 (PICP₉₀ = 0.572)—the dropout-based epistemic uncertainty cannot capture the aleatoric component from limited signal information. Split conformal prediction achieves the best calibration across all parameters (PICP₉₀ \approx 0.90) with provable coverage guarantees, at the cost of wider intervals. Temperature-scaled MC-Dropout offers the best trade-off between calibration and interval width. The deep ensemble is the least calibrated method (PICP₉₀ < 0.58 for all parameters), indicating that random-seed diversity alone is insufficient.

5.7. Validation on Field-Representative Models

Five canonical 1D models spanning published shallow-water MCSEM scenarios (Constable, 2010; Key, 2012) are inverted in a single forward pass with no retraining. Mean absolute percentage error across all parameters and models is 12.1%; σ_1 is recovered to 3–11% and d_1 to 1–6%. The largest d_2 error (46%, model E) occurs at moderate conductivity contrast, consistent with the failure-mode analysis. Full results (Supplement Table S9, Fig. S2) are in Supplement Section S13.

5.8. Step-Off Source Validation

Step-off data require frequency-domain division by $i2\pi f$ before passing to DualTCN. Validation on five field-representative models (Supplement Section S2) shows < 13% prediction differences for $\sigma_2 \gtrsim 0.05$ S/m,

but up to 117% for the highly resistive model D ($\sigma_2 = 0.008 \text{ S/m}$) due to 2 Hz bandwidth truncation. Direct training on step-off waveforms—requiring only dataset regeneration, no architectural changes—is the recommended production path.

5.9. Benchmark Against Published Survey Models

Seven 1D models from published shallow-water MCSEM surveys (Constable and Srnka, 2007; Key, 2009; Constable, 2010; Key, 2012) are inverted in a single forward pass. For moderate-to-high $\sigma_2 \geq 0.3 \text{ S/m}$, MAPE is 7.5%. For resistive targets, the unaugmented model produces large σ_2 errors (up to 1125% at $\sigma_2 = 0.005 \text{ S/m}$); DualTCN-Weighted (inverse- σ_2 sample weighting) reduces overall MAPE from 61.1% to **12.1%**. Full per-site results are in Supplement Section S13 (Supplement Table S10).

5.10. Pseudo-2D Survey Line Demonstration

A synthetic 4 km tow line (200 stations, 50:1 resistive body embedded at 1.2–2.8 km) demonstrates pseudo-2D profiling via station-by-station 1D inference with lateral median filtering. Geometric parameters are well recovered (d_1 MAPE = 3.8%, $R^2 = 0.935$); the resistive body is clearly delineated, though in-body σ_2 MAPE is 47.6%. Full results, figures, and tables are in Supplement Section S14.

6. Discussion

6.1. Architectural Insights

The three best TCN designs form a clear progression: P7 (multi-scale) reduces loss by 9.8% over the TCN-only baseline; P8 (cascaded conditioning) adds 4.2%; DualTCN’s late-time branch and auxiliary d_{sf} head add a further 13.6%, for a cumulative 25.3% improvement ($\bar{R}^2 = 0.877$). The late-time encoder gives the exponential decay regime its own parameters and receptive field, preventing the weak late-time signal from being overwhelmed; the auxiliary head steers gradients toward d_2 -informative features. This branch contributes just 28 K parameters yet provides the largest single gain. Removing the TCN and keeping only the Transformer more than doubles the loss; attention-based encoders (iTransformer, PatchTST) perform $> 2.8\times$ worse despite comparable budgets, because global self-attention conflates the physically distinct early- and late-time regimes (Supplement Section S5). The dilated TCN’s local processing with exponentially growing receptive field is the essential inductive bias for diffusion-governed transients.

6.2. The d_2 Information Bottleneck

Despite DualTCN’s improvement, d_2 remains the hardest parameter ($R^2 = 0.627$ versus > 0.98 for σ_1 and d_1). This difficulty is physical: all four receivers sit within 200 m, so the early- and mid-time response senses mainly the combined depth $d_{\text{sf}} = d_1 + d_2$, not d_1 and d_2 individually. Resolving d_2 requires the low-amplitude late-time tail, where SNR is poor. The narrow physical range (10–50 m, 0.70 log-decades)

further limits the available information. The failure-mode analysis in Section 5.3 confirms that the largest errors cluster among thin layers with weak conductivity contrast—precisely the configurations where the late-time diffusion tail carries the least energy. None of the other modifications we tested—loss re-weighting (P3), capacity expansion (P6), multi-scale coverage (P7), hierarchical conditioning (P8)—raised $R_{d_2}^2$ above 0.56 before DualTCN. Extending the receiver array to 500–1 000 m, where the seafloor geometry is better resolved, is the most promising remedy.

6.3. Comparison with the Literature

DualTCN differs from published DL-CSEM methods (Puzyrev, 2019; Zhang et al., 2024; Zhang and Hu, 2024; Li et al., 2025) in three respects: time-domain input with a physics-motivated dual-branch encoder; parametric output (4–6 scalars) enforced by a differentiable decoder, eliminating non-physical oscillations; and comprehensive amplitude robustness characterisation (five experiments) plus four-method UQ comparison—neither of which has been attempted in prior DL-CSEM work. Inference is a single feedforward pass under 4 ms, qualitatively different from iterative methods (Raissi et al., 2019; Abubakar et al., 2012). The parametric output also enables hybrid workflows: DualTCN’s estimate serves as a warm start for conventional inversion (Section 5.5).

DualTCN’s late-time branch and auxiliary \hat{d}_{sf} head are direct analogues of ATEM strategies (Moghadas, 2020; Liu et al., 2022; Colombo et al., 2021), adapted to the marine setting where conducting seawater and short offsets change the relative importance of early- vs. late-time windows. Generic global attention is poorly suited to MCSEM transients because early- and late-time regimes are not exchangeable; physics-aware hybrid attention is a promising future direction. Extended positioning against alternative paradigms (PGN, DIP-style, ensemble Kalman, probabilistic methods) is provided in Supplement Section S16.

6.4. Three-Layer Extension

A three-layer variant (DualTCN-3Layer, 306 K parameters) trained on a seawater/resistive-layer/basement model demonstrates extensibility: shared parameters transfer with negligible loss (d_1 RMSE improves by 39%), basement conductivity σ_3 is well resolved ($R^2 \approx 0.88$), and d_2 is essentially unchanged (RMSE = 0.170 vs. 0.165). The thin-layer parameters (σ_2 , h) remain resolution-limited ($R^2 \approx 0.45$, 0.23) due to the physical σ_2 - h trade-off at 20–200 m offsets. Full results, equations, and discussion are in Supplement Section S15.

6.5. Uncertainty Quantification Discussion

MC-Dropout is well calibrated for σ_1 (PICP₉₀ = 0.944) but over-confident for d_2 (PICP₉₀ = 0.572), because dropout-based epistemic uncertainty cannot capture the aleatoric component from limited signal information. Temperature scaling and split conformal prediction correct this systematically (Section 5.6). Despite under-coverage, MC-Dropout standard deviation correlates with per-sample error, serving as a triage

signal for follow-up iterative inversion. The 100-pass pipeline costs 350 ms per sample on A100—> 7,000× cheaper than conventional inversion.

6.6. Limitations

Key limitations include: (i) the two-channel input creates a structural amplitude vulnerability mitigated by DualTCN-AmpAug ($\bar{R}^2 = 0.858$ at $\pm 2\%$ noise) and DualTCN-AmpRatio (exact uniform-bias immunity); per-receiver calibration mismatch remains the dominant vulnerability (Section 5.4.1, Fig. 8); (ii) the model requires retraining for different acquisition geometries; (iii) i.i.d. training does not reflect spatial correlation in real surveys; (iv) MC-Dropout under-covers d_2 , correctable by temperature scaling or conformal prediction; (v) no field-data validation is included—amplitude calibration, source-waveform deconvolution, and geometry matching are prerequisites. The 1D assumption limits applicability to laterally uniform geology; the pseudo-2D demonstration (Section 5.10) validates station-by-station inference with lateral smoothing, while 2.5D/3D extensions require different architectures. The retraining pipeline takes < 8 GPU-hours for one million samples; two concrete field-data targets (Zenodo TD-CSEM benchmark, Scarborough gas-field data) are identified for future work.

7. Conclusions

DualTCN is the first deep-learning framework for time-domain multi-receiver marine CSEM inversion. Among 13 architectural variants trained on one million synthetics, its dedicated late-time branch and auxiliary d_{sf} head achieve $\bar{R}^2 = 0.877$ (25.3% loss reduction), with $R_{d_2}^2 = 0.627$. Dilated causal convolution is the essential inductive bias; attention-based encoders perform $2.8\times$ worse.

Curriculum-based amplitude augmentation (DualTCN-AmpAug) mitigates the critical amplitude vulnerability ($\bar{R}^2 = 0.858$ at $\pm 2\%$ noise vs. 0.363 unaugmented; 0.846 at $\pm 5\%$). Inverse- σ_2 weighting reduces published-survey MAPE from 61.1% to 12.1%. A three-layer extension resolves basement conductivity at $R^2 \approx 0.88$ with no architectural changes (Supplement Section S15). MC-Dropout UQ is well calibrated for σ_1 (PICP₉₀ = 0.944); d_2 under-coverage is correctable by temperature scaling or conformal prediction.

DualTCN inverts a sample in 3.5 ms on GPU (8.8 ms CPU), enabling real-time quality control at sea. Against conventional inversion, it achieves $\bar{R}^2 = 0.862$ at 26,500× lower cost. Table 8 provides variant recommendations for five deployment scenarios.

Future priorities include: (i) combining AmpAug and AmpRatio strategies for simultaneous per-receiver and common-mode robustness; (ii) conditional normalising flows for non-Gaussian posterior estimation; (iii) four-layer benchmarks with longer offsets and VTI anisotropy; (iv) spatially correlated evaluation; (v) field-data validation on the Zenodo TD-CSEM benchmark and Scarborough gas-field data.

Data and Code Availability

All training and evaluation data were generated synthetically using `empymod` (Werthmüller, 2017), freely available at <https://empymod.emsig.xyz>. The published survey benchmark (Section 5.9) uses earth-model parameters from Constable and Srnka (2007); Key (2009); Constable (2010); Key (2012). The Scarborough gas-field CSEM data are available at <https://marineemlab.ucsd.edu/Projects/Scarborough/Data.html>. A marine TD-CSEM benchmark dataset is available at Zenodo (doi:10.5281/zenodo.7198873).

Source code, training scripts, configuration files, evaluation pipelines, result data, and trained model weights for all variants reported in this study (DualTCN, DualTCN-AmpAug, DualTCN-Colored, DualTCN-AmpRatio, DualTCN-Weighted, DualTCN-RecvBias, DualTCN-3Layer) are available in a GitHub repository at <https://github.com/Kahmed68/DualTCN> under the MIT open-source license. The repository will be made public upon acceptance; a private reviewer-access link is available from the corresponding author upon request during the review process.

Acknowledgements

This research used resources of the Argonne Leadership Computing Facility (ALCF, Polaris), supported by U.S. Department of Energy Contract DE-AC02-06CH11357.

CRedit Author Statement

Khaled Ahmed: Conceptualization, Methodology, Software, Validation, Formal analysis, Investigation, Data curation, Writing – original draft, Writing – review & editing, Visualization. **Ghada Omar:** Conceptualization, Methodology, Formal analysis, Writing – review & editing, Supervision.

Declaration of Competing Interest

The authors declare that they have no known competing financial interests or personal relationships that could have appeared to influence the work reported in this paper.

References

- Abubakar, A., Habashy, T.M., Li, M., Liu, J., 2012. Inversion algorithms for large-scale geophysical electromagnetic measurements. *Inverse Problems* 28, 123012. doi:10.1088/0266-5611/28/12/123012.
- Angelopoulos, A.N., Bates, S., 2023. Conformal prediction: A gentle introduction. *Foundations and Trends in Machine Learning* 16, 494–591. doi:10.1561/2200000101.

- Araya-Polo, M., Jennings, J., Adler, A., Dahlke, T., 2018. Deep-learning tomography. *The Leading Edge* 37, 58–66. doi:[10.1190/tle37010058.1](https://doi.org/10.1190/tle37010058.1).
- Ardizzone, L., Kruse, J., Wirkert, S., Rahner, D., Pellegrini, E.W., Klessen, R.S., Maier-Hein, L., Rother, C., Köthe, U., 2019. Analyzing inverse problems with invertible neural networks, in: Proc. Int. Conf. Learn. Represent. (ICLR). [Online]. Available: <https://arxiv.org/abs/1808.04730>.
- Bai, P., Vignoli, G., Hansen, T.M., 2024. Unsupervised deep learning magnetotelluric inversion. *Geophysical Journal International* 237, 1–15. doi:[10.1093/gji/ggae005](https://doi.org/10.1093/gji/ggae005).
- Byrd, R.H., Lu, P., Nocedal, J., Zhu, C., 1995. A limited memory algorithm for bound constrained optimization. *SIAM J. Sci. Comput.* 16, 1190–1208. doi:[10.1137/0916069](https://doi.org/10.1137/0916069).
- Colombo, D., Turkoglu, E., Li, W., Sandoval-Curiel, E., Rovetta, D., 2021. Physics-driven deep learning electromagnetic data inversion with applications to subsurface imaging. *Geophysics* 86, B225–B245. doi:[10.1190/geo2020-0759.1](https://doi.org/10.1190/geo2020-0759.1).
- Constable, S., 2010. Ten years of marine CSEM for hydrocarbon exploration. *Geophysics* 75, 75A67–75A81. doi:[10.1190/1.3483451](https://doi.org/10.1190/1.3483451).
- Constable, S., Srnka, L.J., 2007. An introduction to marine controlled-source electromagnetic methods for hydrocarbon exploration. *Geophysics* 72, WA3–WA12. doi:[10.1190/1.2432483](https://doi.org/10.1190/1.2432483).
- Constable, S.C., Parker, R.L., Constable, C.G., 1987. Occam’s inversion: A practical algorithm for generating smooth models from electromagnetic sounding data. *Geophysics* 52, 289–300. doi:[10.1190/1.1442303](https://doi.org/10.1190/1.1442303).
- Gal, Y., Ghahramani, Z., 2016. Dropout as a Bayesian approximation: Representing model uncertainty in deep learning, in: Proc. 33rd Int. Conf. Mach. Learn. (ICML), pp. 1050–1059. [Online]. Available: <https://proceedings.mlr.press/v48/gal16.html>.
- Guo, C., Pleiss, G., Sun, Y., Weinberger, K.Q., 2017. On calibration of modern neural networks, in: Proc. 34th Int. Conf. Mach. Learn. (ICML), pp. 1321–1330. [Online]. Available: <https://proceedings.mlr.press/v70/guo17a.html>.
- Iglesias, M.A., Law, K.J.H., Stuart, A.M., 2013. Ensemble Kalman methods for inverse problems. *Inverse Problems* 29, 045001. doi:[10.1088/0266-5611/29/4/045001](https://doi.org/10.1088/0266-5611/29/4/045001).
- Key, K., 2009. 1D inversion of multicomponent, multifrequency marine CSEM data: Methodology and synthetic studies for resolving thin resistive layers. *Geophysics* 74, F9–F20. doi:[10.1190/1.3058434](https://doi.org/10.1190/1.3058434).
- Key, K., 2012. Marine electromagnetic studies of seafloor resources and tectonics. *Surveys in Geophysics* 33, 135–167. doi:[10.1007/s10712-011-9139-x](https://doi.org/10.1007/s10712-011-9139-x).

- Lakshminarayanan, B., Pritzel, A., Blundell, C., 2017. Simple and scalable predictive uncertainty estimation using deep ensembles, in: *Advances in Neural Information Processing Systems (NeurIPS)*, pp. 6402–6413. [Online]. Available: <https://arxiv.org/abs/1612.01474>.
- LeCun, Y., Bengio, Y., Hinton, G., 2015. Deep learning. *Nature* 521, 436–444. doi:10.1038/nature14539.
- Li, G., et al., 2025. One-dimensional deep learning inversion of marine controlled-source electromagnetic data. *Geophysical Prospecting* doi:10.1111/1365-2478.13622. early access.
- Liu, W., Wang, H., Xi, Z., Zhou, L., 2022. Physics-driven deep learning inversion with application to transient electromagnetic data. *IEEE Trans. Geosci. Remote Sens.* 60, 5901212. doi:10.1109/TGRS.2021.3120138.
- Moghadas, D., 2020. One-dimensional deep learning inversion of electromagnetic induction data using convolutional neural network. *Near Surface Geophysics* 18, 11–32. doi:10.1002/nsg.12030.
- Moré, J.J., 1978. The Levenberg–Marquardt algorithm: Implementation and theory, in: *Numerical Analysis*. Springer. volume 630 of *Lecture Notes in Mathematics*, pp. 105–116. doi:10.1007/BFb0067700.
- Papamakarios, G., Nalisnick, E., Rezende, D.J., Mohamed, S., Lakshminarayanan, B., 2021. Normalizing flows for probabilistic modeling and inference. *J. Mach. Learn. Res.* 22, 1–64. [Online]. Available: <https://jmlr.org/papers/v22/19-1028.html>.
- Puzyrev, V., 2019. Deep learning electromagnetic inversion with convolutional neural networks. *Geophysical Journal International* 218, 817–832. doi:10.1093/gji/ggz204.
- Puzyrev, V., Swidinsky, A., 2021. Inversion of 1D frequency- and time-domain electromagnetic data with convolutional neural networks. *Computers & Geosciences* 149, 104681. doi:10.1016/j.cageo.2020.104681.
- Raissi, M., Perdikaris, P., Karniadakis, G.E., 2019. Physics-informed neural networks: A deep learning framework for solving forward and inverse problems involving nonlinear partial differential equations. *J. Comput. Phys.* 378, 686–707. doi:10.1016/j.jcp.2018.10.045.
- Reichstein, M., Camps-Valls, G., Stevens, B., Jung, M., Denzler, J., Carvalhais, N., Prabhat, 2019. Deep learning and process understanding for data-driven Earth system science. *Nature* 566, 195–204. doi:10.1038/s41586-019-0912-1.
- Sun, J., Li, Y., 2023. Deep image prior for magnetotelluric inversion. *Geophysical Journal International* 235, 2231–2247. doi:10.1093/gji/ggad345.
- Werthmüller, D., 2017. An open-source full 3D electromagnetic modeler for 1D VTI media in Python: empymod. *Geophysics* 82, WB9–WB19. doi:10.1190/geo2016-0626.1.

- Zhang, Z., Hu, Z., 2024. Physics-driven deep-learning for marine CSEM data inversion. *J. Appl. Geophys.* 229, 105497. doi:[10.1016/j.jappgeo.2024.105497](https://doi.org/10.1016/j.jappgeo.2024.105497).
- Zhang, Z., Huang, J., Wan, L., 2024. 3-D CSEM data inversion using deep convolutional neural networks: A feasibility study. *Geophysics* 89, E55–E68. doi:[10.1190/geo2023-0201.1](https://doi.org/10.1190/geo2023-0201.1).
- Zhu, C., Byrd, R.H., Lu, P., Nocedal, J., 1997. Algorithm 778: L-BFGS-B: Fortran subroutines for large-scale bound-constrained optimization. *ACM Trans. Math. Softw.* 23, 550–560. doi:[10.1145/279232.279236](https://doi.org/10.1145/279232.279236).

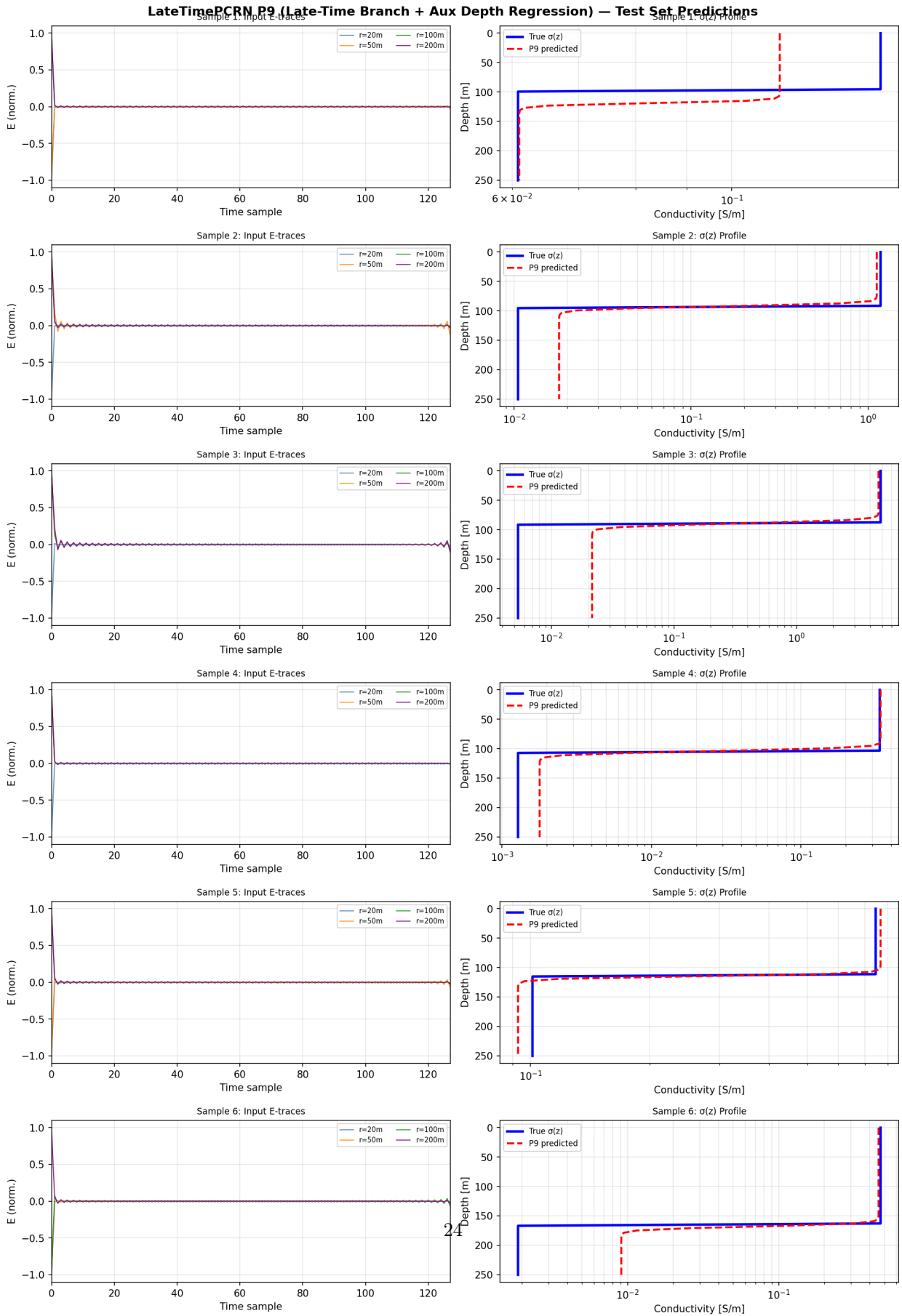


Figure 3: DualTCN predictions on six test samples. Left: normalised E-field traces from four receivers. Right: true profile (blue) and prediction (red dashed).

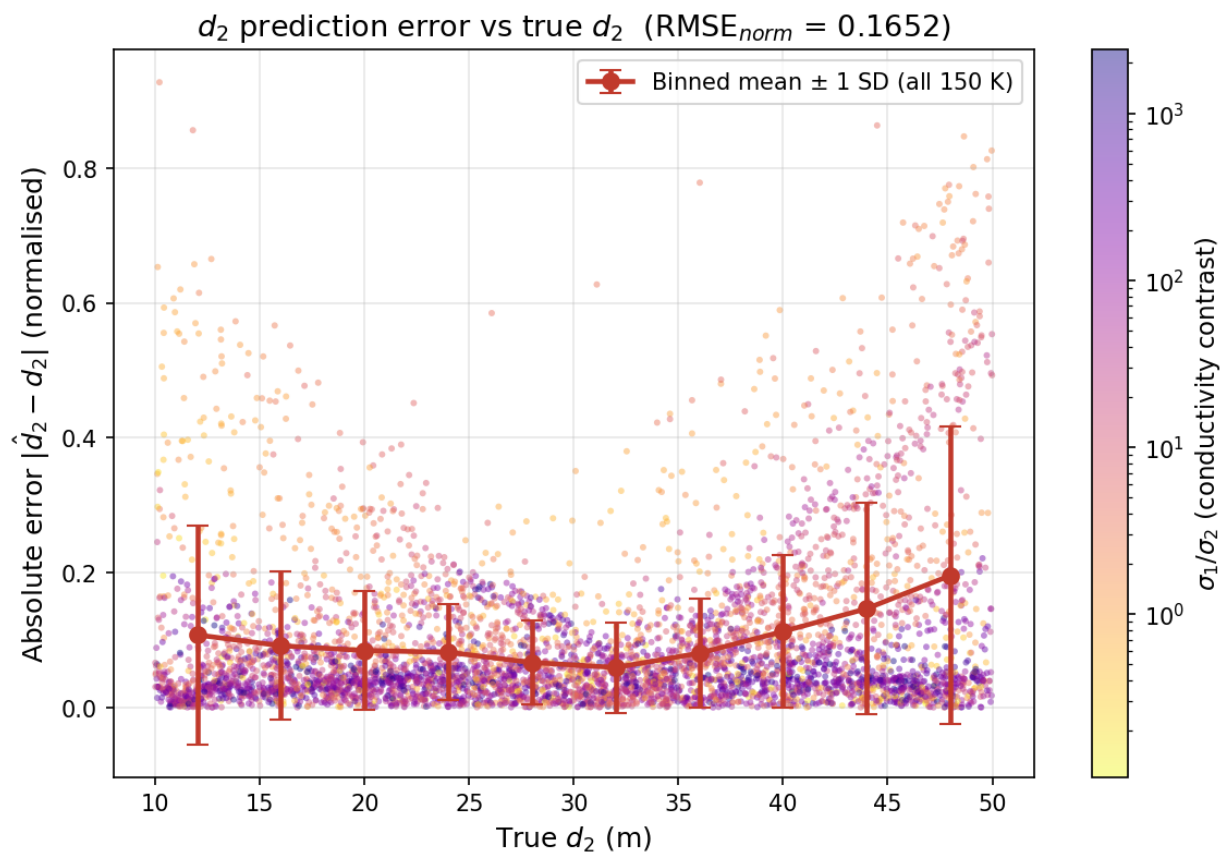


Figure 4: Absolute d_2 prediction error (normalised) versus true d_2 (5 000 test samples), coloured by σ_1/σ_2 . Errors are largest for thin layers with weak contrast (upper-left).

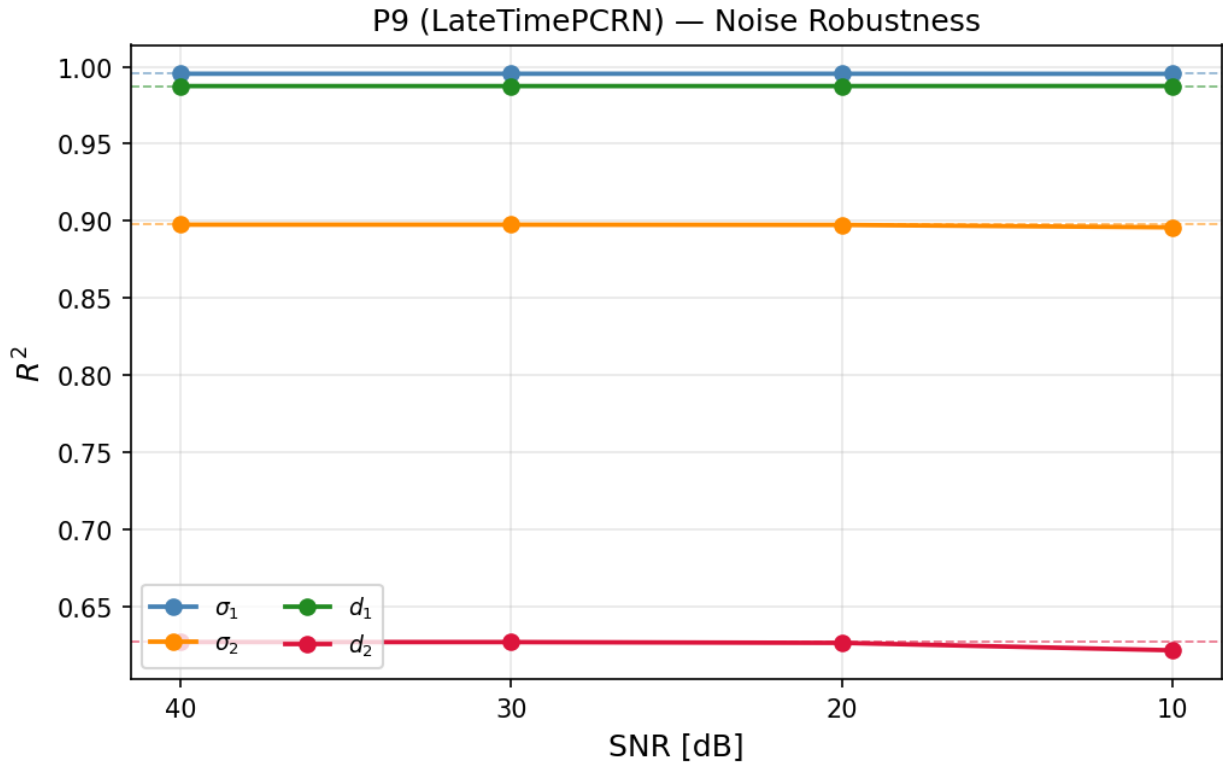


Figure 5: R^2 versus SNR for DualTCN (150 000 test samples). All parameters maintain clean-test values above 20 dB; at 10 dB the worst decline is $\Delta R^2 = 0.005$ (d_2).

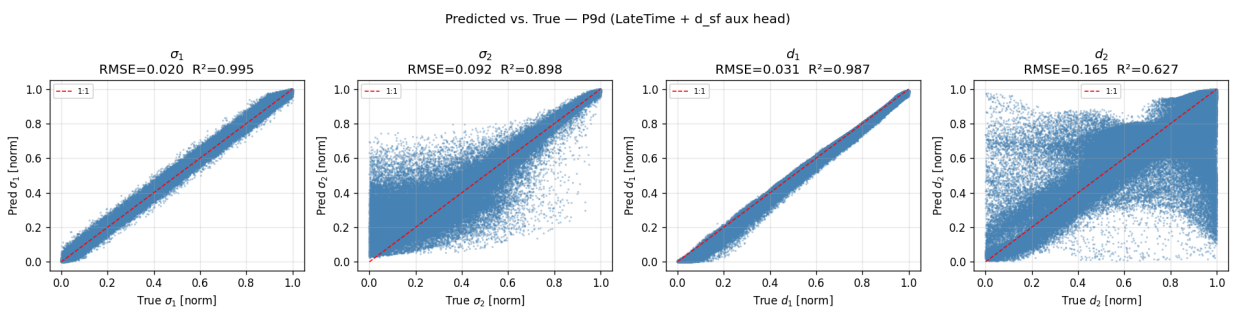


Figure 6: True versus predicted scatter for DualTCN (5 000 test samples, normalised $[0, 1]$ log-space). Dashed line = perfect prediction.

DualTCN sensitivity to amplitude-channel perturbations
(150 000 test samples; waveform channels unperturbed)

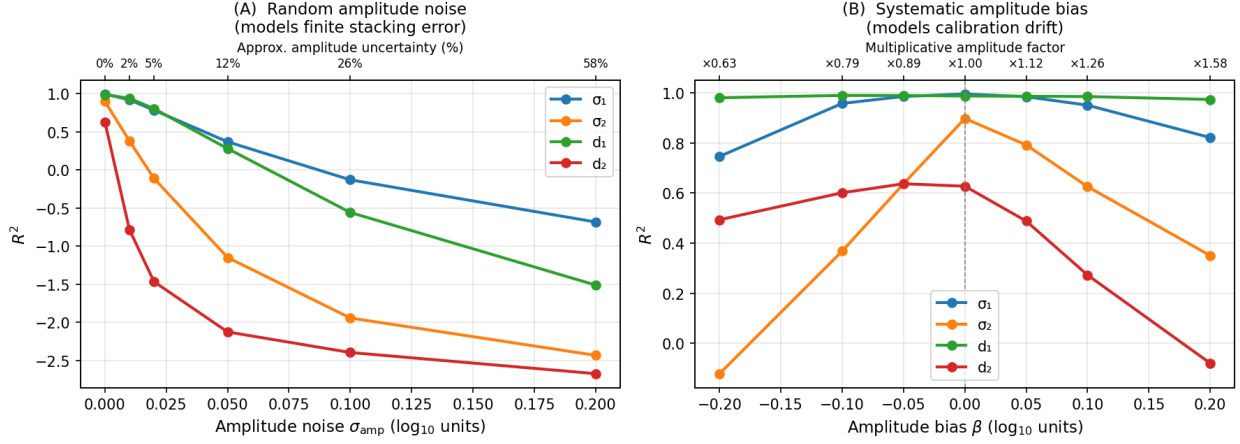


Figure 7: DualTCN R^2 as a function of amplitude-channel perturbation strength (150 000 test samples). Panel (A): random noise σ_{amp} in \log_{10} units (top axis: approximate amplitude uncertainty %). Panel (B): systematic bias β in \log_{10} units (top axis: multiplicative amplitude factor 10^β). In both panels, σ_2 (orange) and d_2 (red) degrade rapidly because they rely primarily on the log-amplitude channel, while d_1 (green) is largely unaffected and σ_1 (blue) occupies an intermediate position.

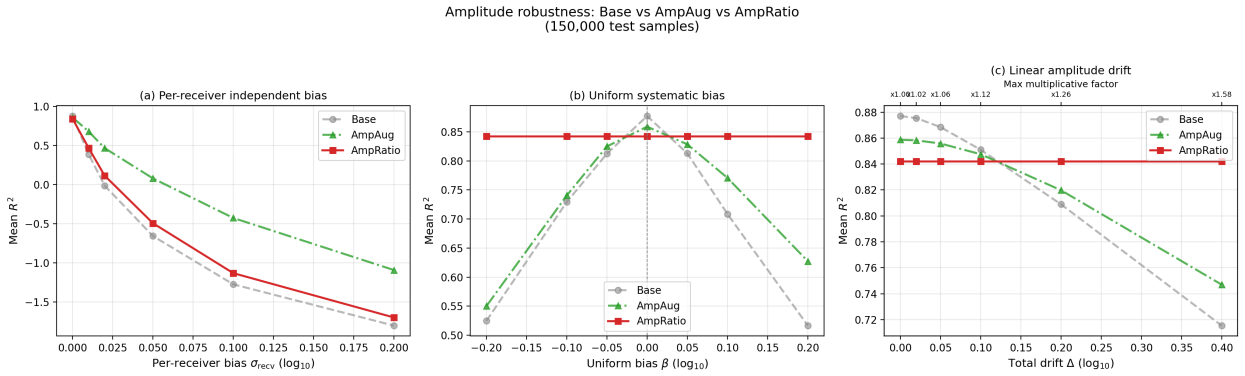


Figure 8: Amplitude robustness of Base, AmpAug, and AmpRatio variants under structured perturbations (150 000 test samples). (a) Per-receiver independent bias: AmpAug is most robust; AmpRatio does not help because independent biases corrupt inter-receiver differences. (b) Uniform systematic bias: AmpRatio is perfectly immune ($\bar{R}^2 = 0.842$ at all $|\beta|$), confirming exact common-mode cancellation. (c) Linear drift (towline simulation): AmpRatio is again perfectly immune; AmpAug overtakes Base at larger drift magnitudes.